AIAA JOURNAL
Vol. 36, No. 10, October 1998

Flowfield Around Ogive/Elliptic-Tip Cylinder at High Angle of Attack

S. C. Luo,* T. T. Lim,* K. B. Lua,† and H. T. Chia‡
National University of Singapore, Singapore 119260, Singapore
and
E. K. R. Goh§ and Q. W. Ho¶
Defence Science Organisation, Singapore 118230, Singapore

We present the results of experimental investigations on the flowfield around a conventional sharp-nose ogive cylinder and an elliptic-tip ogive cylinder. The studies include simultaneous side-force and surface pressure measurements in a wind tunnel as well as flow visualization in a water tunnel. The results show that changes in the direction of the side force are related to changes in the asymmetry of the pressure distribution along the body. Of the two tip shapes investigated, it is found that the variation of the side force with the roll angle for the elliptic tip is more predictable than that for the sharp ogive tip. Although the flow visualization study shows that the elliptic-tip cylinder with the major axis transverse to the freestream is more effective in delaying the onset of flow asymmetry to a higher angle of attack, the maximum side forces for the two tip geometries are almost the same.

Nomenclature

C_p = pressure coefficient, $(P - P_\infty)/(0.5\rho U_\infty^2)$
C_y = side-force coefficient, $Fy/(0.5\rho U_\infty^2 S)$
C_{yD} = local side-force coefficient, local side force$/(0.5\rho U_\infty^2 D \sin^2\alpha)$
D = cylinder diameter
F_y = side force
L = length of body
P = pressure on model surface
P_∞ = freestream static pressure
Re_D = Reynolds number, $U_\infty D/\nu$
S = model base area, $\pi D^2/4$
U_∞ = freestream velocity
X = axial distance from nose tip
α = angle of attack
δ_N = tip semiapex angle
θ = azimuth angle around circular cross section measured from the most leeward position
ν = kinematic viscosity of fluid
ρ = density of fluid
ϕ = roll angle

I. Introduction

It is well known that, when an aircraft or missile is flying at high angle of attack, vortices generated on the forebody can become asymmetric, leading to the generation of a large side force on the forebody. Previous studies have shown that the side force can be as large as 1.5 times the normal force on the forebody.[1,2] Moreover, under this operating condition, traditional control surfaces are found to be ineffective in overcoming the yawing moment created by the side force because they are likely to be engulfed in the wakes of the wings and forebody. This may result in the loss of control of the flight vehicle.

At present, there are two different methods of handling the side-force problem. The first method is aimed at keeping the side-force magnitude to a minimum by either inducing symmetric separation or destroying the coherence of the forebody vortices. The second method is to make use of the yawing moment generated by the forebody vortices to provide directional control to the flight vehicles. Devices that have been used in the first method include 1) the symmetric strakes,[3,4] or active devices to create either blowing or suction[4–6] to induce symmetric separation at the two sides of the forebody; 2) the helical[7] or boundary-layer trip,[8,9] which is used to prevent the formation of strong coherent leeward vortices, resulting in a dramatic decrease in the side force; and 3) the small single strake at the leeward position of the nose[10,11] or just at the tip.[12] The idea here is to prevent the two wake vortices from crowding together, a situation that is thought to be responsible for hydrodynamic instability and hence flow asymmetry.[13] In the second method, the objective is to make use of the yawing moment generated by the forebody vortices to provide directional control. This method has been suggested as a possible replacement for the traditional directional control devices that have lost their effectiveness at high angle of attack. Some of these devices include movable strakes[5,14] and blowing or suction[5,6] through holes or slots, as well as rotatable tip strakes.[5,6,15] All of these devices work on creating asymmetric leeward vortices of the desired strength and orientation by manipulating the boundary-layer separation on each side of the body. These techniques show promise but are restricted by practical constraints, such as space availability near the nose of the aircraft.

From the preceding discussion, it is highly desirable to have forebody vortex control devices that not only are simple in design but also have no protruding parts. An elliptic nose tip has been suggested as a possible way to meet these requirements. Previous studies have shown that the geometry of the elliptic tip plays a dominant role over the surface roughness and microgeometrical imperfections, which are thought to be responsible for the generation of asymmetric vortices[16–19] and hence the side force on a sharp-nose ogive cylinder. In other words, the side forces generated on an elliptic nose are more predictable, and at the same time, the force magnitudes and yawing moment are lower. These effects translate into better directional stability for the flight vehicle. One example of such a nose shape used in actual aircraft is the shark nose of the F-5F fighter aircraft.[20]

Recently, a number of researchers have been working on the aerodynamic characteristics of the elliptical nose; see, for example, Refs. 21–23. In their studies, Moskovitz et al.[21,22] noted that, at moderate angle of attack, the elliptical tip that they were using was successful in generating a smooth two cycles of sinusoidal variation in the local side force per 360 deg of roll. However, at very high angle of attack, i.e., $\alpha \geq 40$ deg for cone and $\alpha \geq 60$ deg for ogive nose, a

---

Received Aug. 27, 1997; revision received May 11, 1998; accepted for publication May 20, 1998.

*Senior Lecturer, Department of Mechanical and Production Engineering.

†Research Assistant and Postgraduate Student, Department of Mechanical and Production Engineering.

‡Graduate Student, Department of Mechanical and Production Engineering.

§Senior Engineer, Aeronautics Laboratory.

¶Principal Engineer, Aeronautics Laboratory.

bistable state in the side force is formed. Here, the side force exhibits a square-wave-like behavior and changes its direction abruptly over approximately every 90 deg of roll angle. More recently, Bridges and Hornung[23] designed an elliptical tip that merged gradually with a right circular cone. Their results showed that, for angles of attack below 39 deg, the variation of side force with roll angle is approximately sinusoidal but becomes square wave like when $\alpha \approx 39$ deg. At even higher angles of attack of 45 and 49 deg, they found a large fluctuation superimposed onto the square-wave-like side-force distribution. On some occasions, these large fluctuations may be large enough to cause a change in the direction of the side force. From their flow visualization, Bridges and Hornung[23] noted that the variation in C_y described is caused by the vortex breakaway, which allows a vortex from one side of the body to cross over to the other side. They also found that, before the breakaway location, the positions of the vortices varied little and the variation of the local side force with the roll angle is smooth. Both Moskovitz et al.[21,22] and Bridges and Hornung[23] concluded that the elliptical cross-section tip shows good potential as a device to provide directional control for flight vehicles.

With the preceding research findings in mind, the objectives of the present investigation are twofold.

1) To conduct detailed studies of the flowfield around a sharp-nose ogive cylinder. Particular attention is focused on simultaneous measurements of the side force and the associated pressure distributions on the forebody. This is in contrast to the previous studies, which concentrated mainly on either side-force or pressure measurements alone. The authors are not aware of any simultaneous side-force and pressure measurements ever reported in the literature.

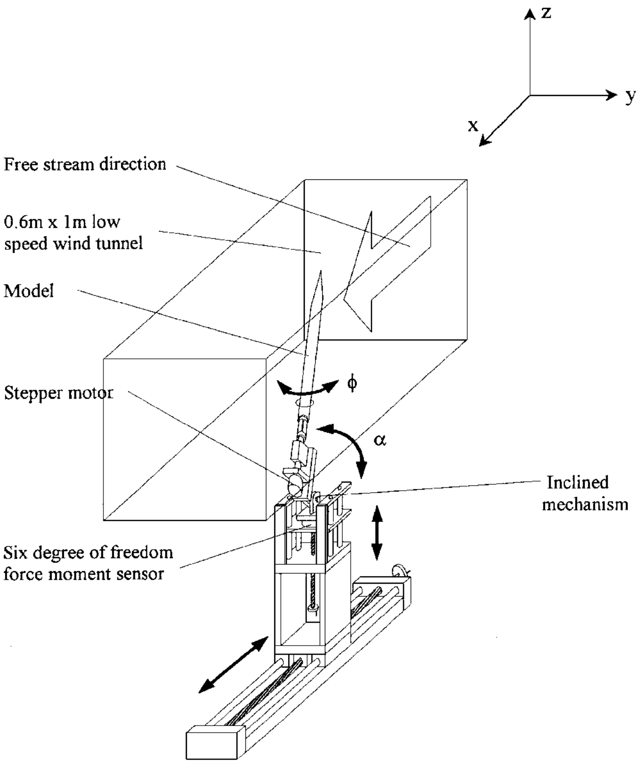

Fig. 1 Schematic diagram of experimental setup.

2) To repeat the same measurements for the elliptical tip. Here, comparisons are made with the results from the sharp-nose ogive cylinder.

The organization of the paper is as follows: The experimental apparatus and approach are presented in Sec. II. This is followed by the results and discussions in Sec. III and the conclusion in Sec. IV.

II. Experimental Apparatus and Techniques

The experiments were carried out in the National University of Singapore's 0.6-m-high × 1.0-m-wide test-section, low-speed wind tunnel. Figure 1 shows the schematic drawing of the setup together with the coordinate system used. All measurements were conducted at a freestream velocity of 15 m/s with the turbulence intensity ≈0.23%, thus giving a Reynolds number based on the diameter ($D = 35$ mm) of the cylindrical section of the model (Re_D) of 3.5×10^4. At this operating condition, the boundary layer involved is likely to be laminar.[24]

The two models were fabricated from aluminum. One has the usual sharp-tip ogive nose (Fig. 2), and the other has part of the ogive nose replaced by an elliptical tip (Fig. 3). The two models are identical except for the first 60 mm from the sharp end, which is referred to as the tip. For the ogive tip, the tip half-apex angle δ_N is 16.26 deg, whereas for the elliptic tip, the cross-sectional shape changes gradually from an elliptic geometry to a circular shape that merges with the ogive nose at 60 mm from the tip. The elliptical tip is based on a design similar to the one adopted by Bridges and Hornung,[23] except that, in the present experiment, it is fitted on the ogive nose instead of on a cone. The minor axis of the ellipse follows a sixth-degree polynomial $X = C_6R^6 + C_5R^5 + C_4R^4 + C_3R^3 + C_2R^2 + C_1R + C_0$, where X is the axial distance measured from the sharp end and R is the local minor axis. The major axis also follows a sixth-order polynomial (but with different coefficients) for the first 20 mm from the tip but, between 20 and 60 mm, it is fitted with a straight line of the form $X = K_1R + K_2$. The coefficients of the equations are chosen so that there is no discontinuity in the gradient at all meeting junctions.

Both models have a nose length of $3.5D$ and a body length of $12.5D$, where D is the (constant) diameter of the cylindrical section of 35 mm. During fabrication, great care was taken to ensure a smooth transition from the nose to the body. Pressure tappings are located at $1.5D$, $2D$, $3D$, $4D$, $5D$, and $6D$ from the sharp end of the model. There are 4 pressure tappings (90 deg apart) at the first station, 8 tappings (45 deg apart) at the second station, and 16 tappings (22.5 deg apart) at the other stations. A total of 76 tappings (maximum allowable in the model) were used, and positions of the pressure stations are designed to cover at least the first local side-force peak.[25] All pressure measurements were carried out using two sets of 48-channel Scanivalve® equipped with ±0.3-psi pressure transducers with an accuracy of ±0.2% of the full scale. This translates into a maximum error of ±0.037 for the pressure coefficient at a freestream wind speed of 15 m/s.

Figure 4 defines the sign convention used for the side force, the roll direction of the model ϕ, and the azimuth angle θ. Here, the

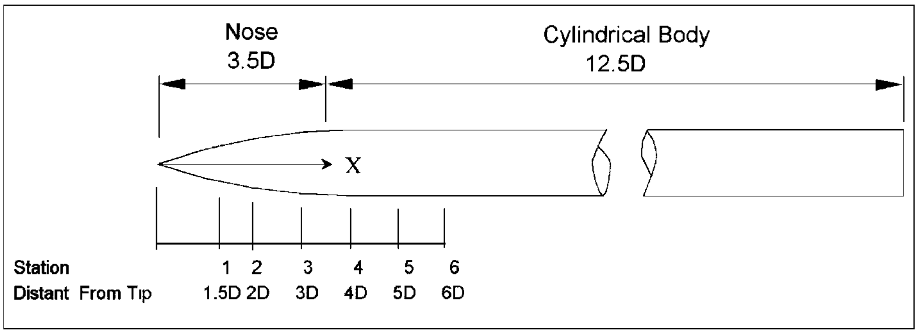

Fig. 2 Position of pressure taping stations on the model.

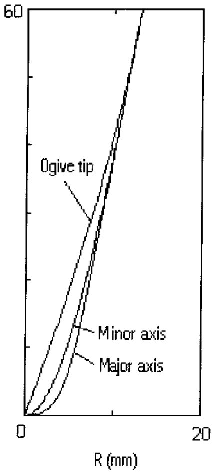

Fig. 3a Axial variation of the ogive tip together with the major and minor axes of the elliptical tip.

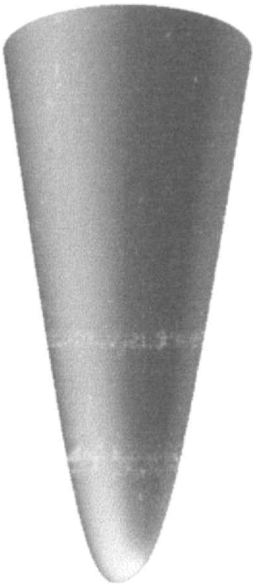

Fig. 3b Elliptical tip.

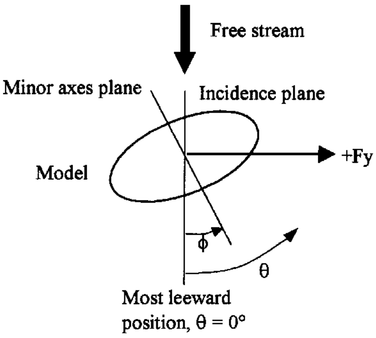

Fig. 4 Definitions of side force F_y, roll angle ϕ, and azimuth angle θ.

positive side force is always pointed toward the starboard side of the body, i.e., in the positive y direction of the coordinate system that is fixed with respect to the wind tunnel (see Fig. 1). The zero azimuth angle is always located at the most leeward position, and the azimuth angle increases in a counterclockwise direction (when view from the top). Note that the azimuth angle also is fixed with respect to the wind tunnel.

To measure the variation of the side force with the roll angle, the model was rotated in a counterclockwise direction by a software-controlled stepper motor located behind the model. Both the model and the stepper motor are mounted on an inclined mechanism, which in turn is mounted on a Nitta six-degree-of-freedom force balance. The accuracy of the balance is ±1.16 g, which corresponds to a maximum error of ±0.0891 for the side-force coefficient at the operating speed of 15 m/s. The length of the model inside the wind tunnel is designed to be adjustable so that measurements can be carried out with different aspect ratios (length-to-diameter ratios) of the model. The inclined mechanism mentioned earlier was designed so that the angle of attack α (the pitch angle) of the model can be varied from 20 to 80 deg.

An IBM computer equipped with an Intel 486 microprocessor was used to both acquire the data and control the stepper motor. During a typical data acquisition routine, after the model had been rotated by the steeper motor to a new roll angle, a 2-s delay was allowed for the flow to stabilize before force measurements were taken at a sampling frequency of 1 kHz over 10 s. This was followed by pressure measurements of all 76 pressure tappings, with 5000 data collected at each pressure tap. Because of the limitation of the data acquisition card, pressure measurements had to be carried out in a sequential manner using two sets of Scanivalve. After the completion of the data acquisition, all results were time averaged and stored on a hard disk before the model was rotated to the next roll angle, and the preceding process then was repeated. Unless otherwise stated, for each angle of attack, measurements were carried out over the entire 360-deg roll angle at 7.2-deg increments.

III. Results and Discussion

The side-force coefficient distribution of the ogive- and elliptical-tip models at different angles of attack α are presented in Fig. 5, with α increases from the top to the bottom of the figure. Figures 6–14 show the corresponding pressure and local side-force distributions for the two models at different α and roll angle ϕ. For easy comparison, pressure distribution for all of the pressure measuring stations at a given ϕ and α are presented in the same figure. The flow visualization results are shown in Figs. 15 and 16.

A. Ogive-Tip Results

For the ogive-tip cylinder, the side force is practically zero at $\alpha = 20$ deg (Fig. 5Aa) and remains very small at $\alpha = 25$ deg (Fig. 5Ab) throughout the entire range of the roll angle. This behavior is consistent with the limited circumferential pressure distribution presented in Fig. 6, which shows that the flow is in fact symmetrical at all six axial positions, even at the location of maximum local side force ($\phi = 295.2$ deg; Fig. 5Ab). At this point, the authors stress that the pressure tappings were positioned in such a way that they encompass at least the first half cycle of the axial side-force variation. They are based on the earlier results of Lamont and Hunt.[25] However, because of the limited number of pressure measurements obtained in this study, one should keep in mind that the pressure data do not give a complete picture of the entire pressure field on the body. Therefore, any attempt to directly relate the pressure field with the global force measurements should be carried out with great caution.

As α increases, it is found that the magnitude of the side force also increases. At $\alpha = 30$ deg, the side-force distribution can be seen to vary with the roll angle in a continuous manner (Fig. 5Ac). The pressure distribution corresponding to the maximum side force in Fig. 5Ac, i.e., at $\phi = 50.4$ deg, is plotted in Fig. 7. Here, it can be seen that there is a flow asymmetry at the last three measuring stations. This finding is consistent with the suggestion by Keener and Chapman[1] that flow asymmetry propagates from the downstream end of the body toward the tip and will reach the nose only when $\alpha = \alpha_{\text{onset}} \approx 2\delta_N$, where δ_N is the tip semiapex angle. In the present study, δ_N is approximately 16 deg, which means that α_{onset} should be about 32 deg. Close examination of the results at $\alpha = 30$ deg shows that the pressure asymmetry can be detected only at the fourth to sixth stations, which are in the vicinity of the nose/body junction.

At $\alpha = 40$ deg, the side force increases further and the asymmetry in the pressure distribution has reached the nose tip. In addition, the side force now exhibits a square-wave-like variation with the roll angle (Fig. 5Ad). The switchover between the positive and negative amplitude is abrupt, and its location is unpredictable but repeatable. The pressure distribution corresponding to the maximum and zero side force at $\phi = 50.4$ and 244.8 deg (points i and ii in Fig. 5Ad) are shown in Figs. 8a and 8b, respectively. In Fig. 8a, it can be seen that the asymmetry in the pressure distribution starts to become distinct from the second station and reaches a maximum at

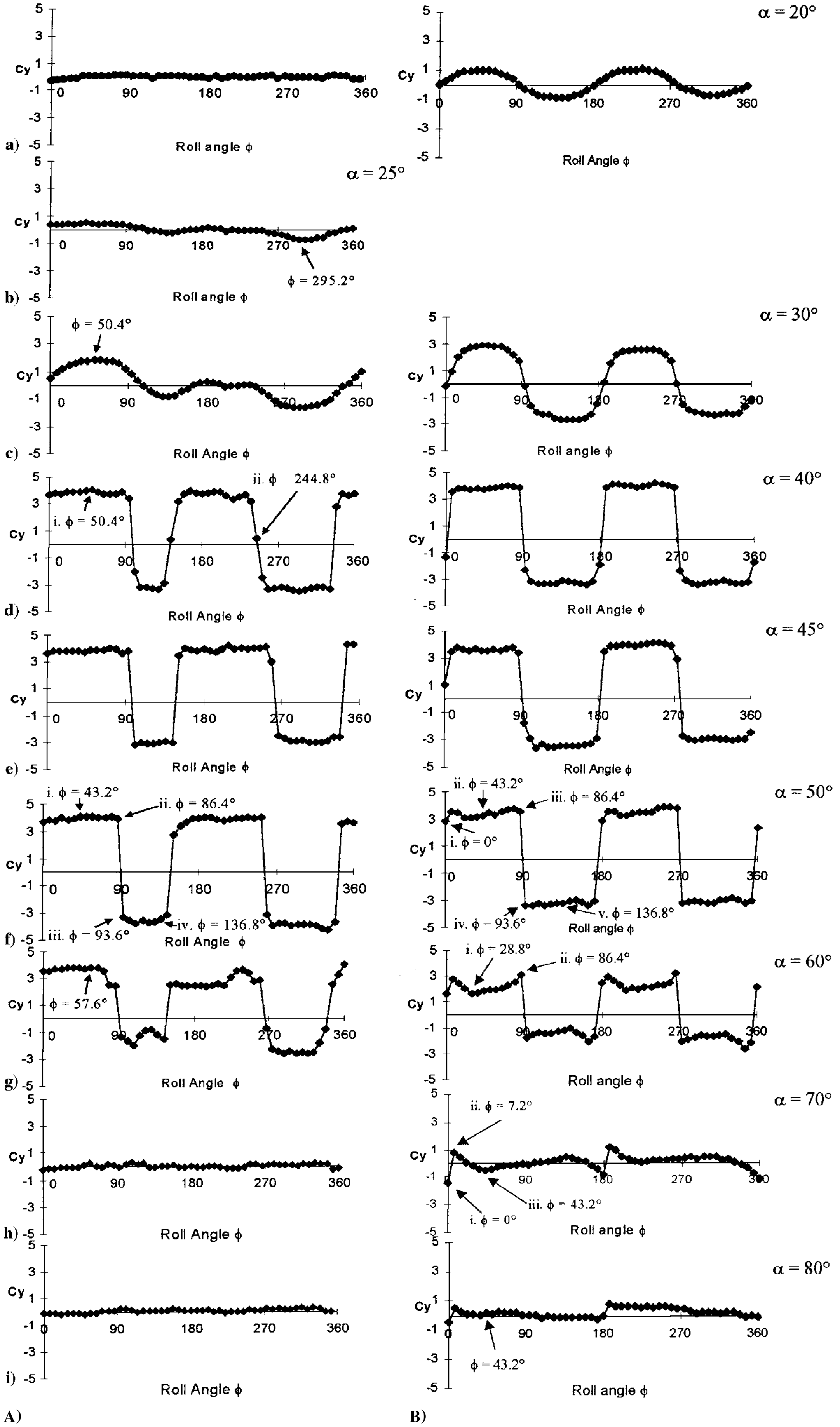

Fig. 5 Side-force coefficient vs roll angle for A) the ogive tip and B) the elliptical tip model at various α.

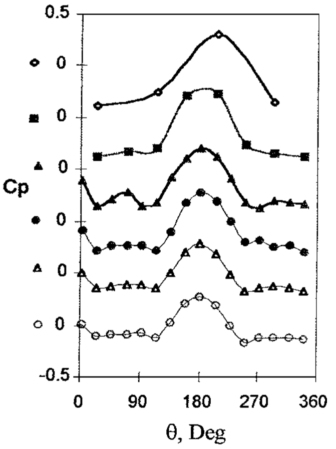

Fig. 6 Pressure coefficient vs θ for ogive-tip cylinder at ϕ = 295.2 deg and α = 25 deg: ◇, station 1; ■, station 2; ▲, station 3; ●, station 4; △, station 5; and ○, station 6.

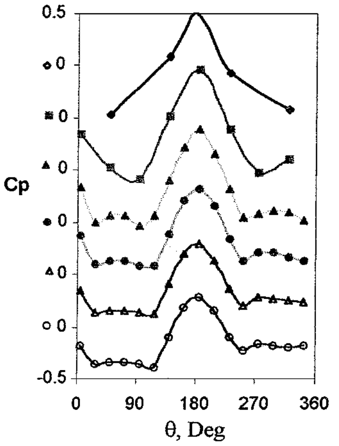

Fig. 7 Pressure coefficient vs θ for ogive-tip cylinder at ϕ = 50.4 deg and α = 30 deg: symbols as in Fig. 6.

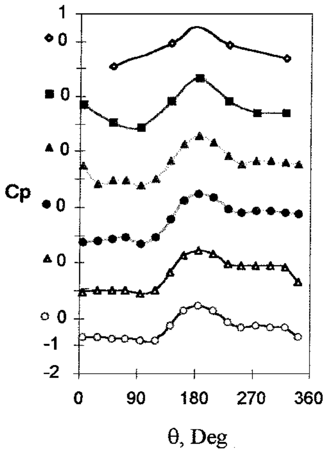

Fig. 8a Pressure coefficient vs θ for ogive-tip cylinder at ϕ = 50.4 deg and α = 40 deg: symbols as in Fig. 6.

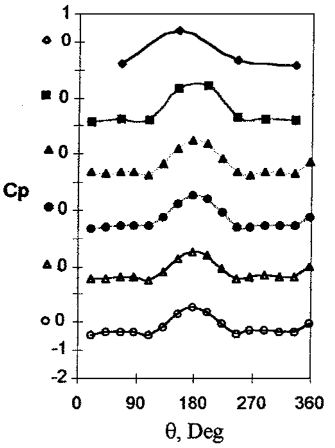

Fig. 8b Pressure coefficient vs θ for ogive-tip cylinder at ϕ = 244.8 deg and α = 40 deg: symbols as in Fig. 6.

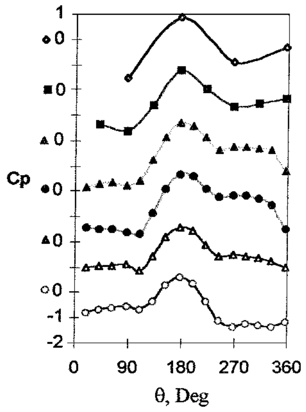

Fig. 9a Pressure coefficient vs θ for ogive-tip cylinder at ϕ = 86.4 deg and α = 50 deg: symbols as in Fig. 6.

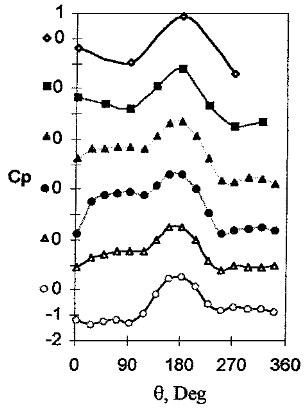

Fig. 9b Pressure coefficient vs θ for ogive-tip cylinder at ϕ = 93.6 deg and α = 50 deg: symbols as in Fig. 6.

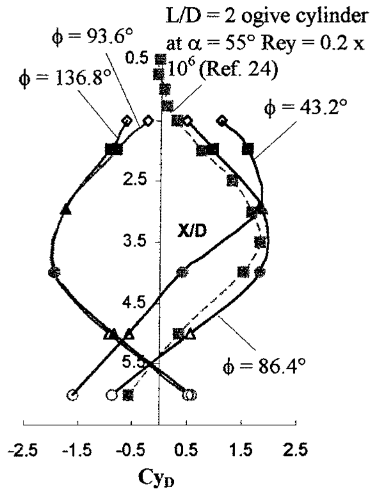

Fig. 9c Local side-force coefficient distributions vs *X/D* for ogive-tip cylinder at ϕ = 43.2, 86.4, 93.6, and 136.8 deg and α = 50 deg together with results from Ref. 24: symbols as in Fig. 6.

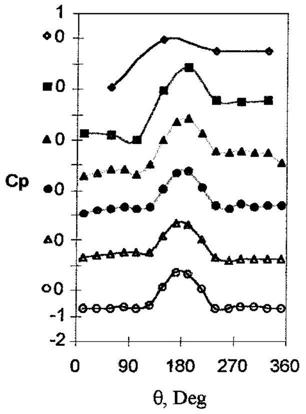

Fig. 10 Pressure coefficient vs θ for ogive-tip cylinder at ϕ = 57.6 deg and α = 60 deg: symbols as in Fig. 6.

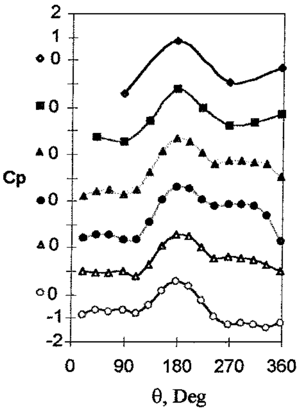

Fig. 11a Pressure coefficient vs θ for elliptic-tip cylinder at ϕ = 86.4 deg and α = 50 deg: symbols as in Fig. 6.

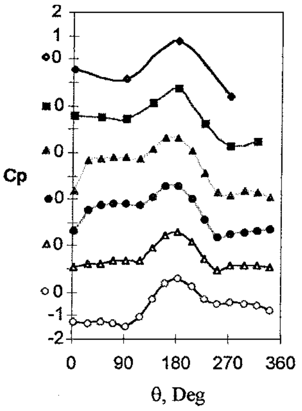

Fig. 11b Pressure coefficient vs θ for elliptic-tip cylinder at ϕ = 93.6 deg and α = 50 deg: symbols as in Fig. 6.

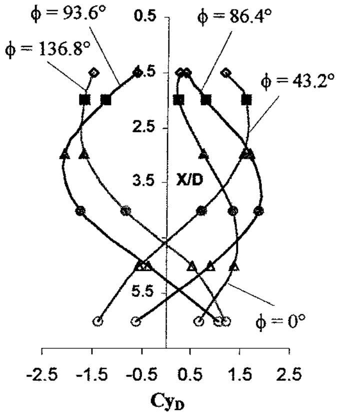

Fig. 11c Local side-force distributions vs X/D for elliptic tip at ϕ = 0, 43.2, 86.4, 93.6, and 136.8 deg and α = 50 deg: symbols as in Fig. 6.

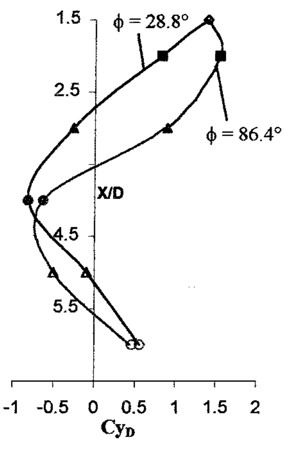

Fig. 12 Local side-force distributions vs X/D for elliptic-tip cylinder at α = 60 deg: symbols as in Fig. 6.

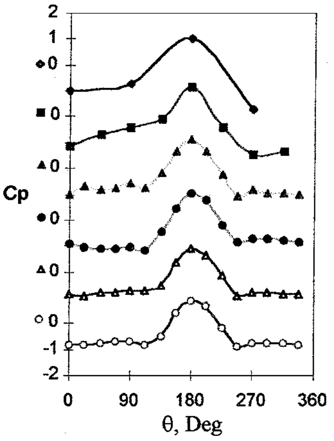

Fig. 13a Pressure coefficient vs θ for elliptic-tip cylinder at ϕ = 0 deg and α = 70 deg: symbols as in Fig. 6.

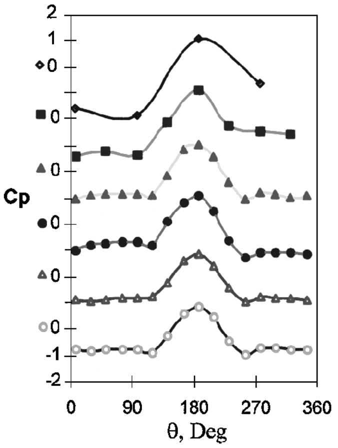

Fig. 13b Pressure coefficient vs θ for elliptic-tip cylinder at ϕ = 7.2 deg and α = 70 deg: symbols as in Fig. 6.

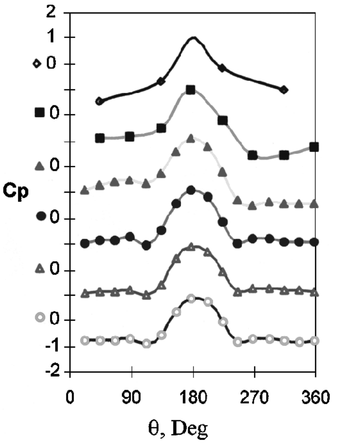

Fig. 13c Pressure coefficient vs θ for elliptic-tip cylinder at ϕ = 43.2 deg and α = 70 deg: symbols as in Fig. 6.

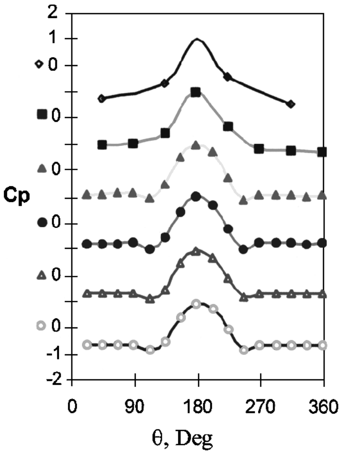

Fig. 14 Pressure coefficient vs θ for elliptic-tip cylinder at ϕ = 43.2 deg and α = 80 deg: symbols as in Fig. 6.

the fifth station. At this roll angle, i.e., 50.4 deg, the local side force varies in a sinusoidal manner along the axial direction. On the other hand, in Fig. 8b, where $\phi = 244.8$ deg, the pressure distribution for all six stations shows little if any asymmetry. This is consistent with the near-zero side force indicated as point ii in Fig. 5Ad. At this roll angle, there is no evidence of axial variation of the side force. When α is increased to 45 and 50 deg (Figs. 5Ae and 5Af, respectively), the side-force magnitude is similar to that at $\alpha = 40$ deg except that the switching between the positive and negative magnitude occurs abruptly and no intermediate point could be captured. Note that, although the averaged side force within each of the two bistable states appears to be insensitive to changes in the roll angle, the local side-force distributions are found to be a function of the roll angle. In Fig. 9c, the local side-force distributions at $\alpha = 50$ deg and $\phi = 43.2$, 86.4, 93.6, and 136.8 deg corresponding to points i–iv in Fig. 5Af, respectively, are presented. At $\phi = 43.2$ and 86.4 deg, the total side forces (measured by force balance) at these two locations are similar in direction and magnitude, although their corresponding local distributions, calculated from integration of local circumferencial pressure distribution, are not the same. At $\phi = 43.2$ deg, it is found that the magnitude of the local side force increases near the tip, and the crossover to the opposite side occurs earlier than the corresponding one at $\phi = 86.4$ deg. Close examination of these roll angles shows that, although the case of $\phi = 43.2$ deg has a larger initial asymmetry, its short axial extent results in the overall side force that is similar in magnitude to that when $\phi = 86.4$ deg. However, it is found that there are some roll angles where both the total side-force and the local side-force distributions are similar. One such example can be found at $\alpha = 50$ deg with $\phi = 93.6$ and 136.8 deg. This phenomenon also was observed by Lamont,[24] who obtained both his total and local side-force distributions by integrating the surface pressure distributions. For the purpose of comparison, the result of Lamont[24] for an ogive cylinder with a fineness ratio of $2D$ also is plotted in Fig. 9c. The angle of attack and the Reynolds number in Lamont's result are 55 deg and 2×10^5, respectively. It can be seen from Fig. 9c that our results at $\phi = 86.4$ deg compare reasonably well with those of Lamont's, except that the side-force magnitude in Lamont's case is slightly smaller. This could be due to the smaller nose aspect ratio used in his investigation.

At $\alpha = 60$ deg (Fig. 5Ag), the side-force variation with the roll angle still exhibits a square-wave-like behavior but with more superimposed distortions and a smaller average magnitude. The pressure distribution at $\phi = 57.6$ deg, which corresponds to the maximum side force at $\alpha = 60$ deg, is shown in Fig. 10. It is observed that the asymmetry in the pressure distribution occurs only in the first three stations. By the fourth station, the pressure distribution appears symmetrical and resembles that of a normal circular cylinder in uniform flow. At $\alpha \geq 70$ deg, the side force becomes negligibly small (Figs. 5Ah and 5Ai). All pressure distributions (not shown for brevity) are symmetrical and resemble the pressure distribution on a circular cylinder in uniform flow.

B. Elliptic-Tip Results

The side-force distribution for the elliptic-tip cylinder is shown in Fig. 5B, and the corresponding pressure distributions for the six axial positions are shown in Figs. 11–14. Note that $\phi = 0$ deg corresponds to the orientation when the elliptic tip is aligned with its major axis transverse to the freestream direction, i.e., symmetrical about the center plane.

Compared with the sharp-tip ogive model (Fig. 5A), it is clear that the elliptic tip shows quite different side-force characteristics. In fact, when $\alpha = 20$ deg (Fig. 5Ba), the side force already has developed quite substantially. As the angle of attack is increased further to $\alpha = 30$ deg, the side-force distribution first exhibits a sinusoidal trend (Fig. 5Bc), followed by a bistable (square-wave-like) trend when α is between 40 and 60 deg. Note that, when a bistable state is reached at $\alpha = 40$ deg (Fig. 5Bd), the positive and negative side forces are approximately equal in magnitude, with each remaining nearly constant over an entire roll-angle range of 90 deg. Interestingly, it is found that the side-force magnitude on the elliptic tip is approximately the same as that on the ogive tip, despite the marked difference in their geometries. This finding, of course, is not new and has been noted by Bridge and Hornung.[23] However, unlike the ogive-tip nose, the switchover position between the high (positive) and low (negative) value is more predictable for the elliptic tip and is found to take place at around $\phi = 0$, 90, 180, and 270 deg. For ease of reference, these roll angles are henceforth referred to as switching ϕ.

For completeness, the authors decided to examine the local side-force distributions at $\phi = 0$, 43.2, 86.4, 93.6, and 136.8 deg at $\alpha = 50$ deg (see points i–v in Fig. 5Bf). The first three ϕ correspond to a nearly constant-magnitude positive side force, whereas the last two correspond to a nearly constant-magnitude negative side force. At $\phi = 0$ deg, it can be seen in Fig. 11c that the local side-force peak is relatively low, which could mean that the flow is not highly asymmetric when the major axis of the tip is aligned transverse to the flow. However, the lower peak is compensated by a larger extent of positive local side force in the axial direction. Consequently, this produces a net overall positive side force. At $\phi = 43.2$, 86.4, 93.6, and 136.8 deg, the local side-force distribution is found to change with the roll angle and the positive and negative side-force distribution are nearly mirror images of each other.

When $\alpha = 60$ deg, there is a slight dip in the side-force distribution on each of the two stable states. Also, it is found that the maximum side force occurs at every 90 deg, i.e., immediately before and after the side force changes sign, and the overall mean value is lower (Fig. 5Bg). Note that, when the body is at its most asymmetric configuration relative to the flow (e.g., $\phi = 45$ deg, 135 deg), the side force appears to have a smaller magnitude than when the body is at a more symmetric configuration. For comparison, the local side-force distributions corresponding to a minimum and maximum side force (points i and ii in Fig. 5Bg, where $\phi = 28.8$ and 86.4 deg, respectively) are shown in Fig. 12. Here it can be seen that, at $\phi = 28.8$ deg, the local side force changes sign at a smaller axial distance from the tip. This implies that the first vortex pair may have lifted from the body earlier compared with $\phi = 86.4$ deg. Also, the smaller side force observed at the nonswitching ϕ, e.g., $\phi = 28.8$ deg, may be a consequence of the early breakaway of the first vortex pair. Based on the pressure distributions (not shown for brevity) at the maximum and minimum side-force positions, i.e., $\phi = 86.4$ and 28.8 deg, respectively, it appears that the asymmetry of the vortices persists for a larger axial distance for these two conditions compared to similar conditions on the ogive-tip model.

In relation to the results of Bridge and Hornung[23] for the cone model and Moskovitz et al.[21,22] for the ogive model at high angle of attack, it can be seen that the present findings agree rather well with theirs. However, what is new in the present study is that the authors are able to determine and present the axial variation of local side force, which the previous work did not. It is believed that this will give better insights into the flow structure under investigation.

Based on the present results, it appears that having an elliptical tip alone is not sufficient to control the side-force magnitude at high angle of attack. Tajfar and Lamont[26] show that a completely elliptical cylinder may be a better choice to eliminate the bistable side-force state completely, although they found that the change in the side force can be quite abrupt at certain ϕ.

At $\alpha = 70$ deg, it is found that the side-force distribution is no longer square wave like, and its magnitude is close to zero except when ϕ is near 0 and 180 deg, where sudden changes in the side force from a negative to a positive value can be seen (Fig. 5Bh). For comparison, the pressure distributions corresponding to the minimum and maximum side forces as well as the local minimum side force at $\phi = 0$, 7.2, and 43.2 deg (points i–iii in Fig. 5Bh) are shown in Figs. 13a, 13b, and 13c, respectively. In Figs. 13a and 13b, one can see quite clearly the asymmetry in the pressure distribution in the first, second, and fourth stations. However, it is quite obvious that the asymmetry in the fourth station is opposite to that of the first two, which implies a possible variation in the direction of the local side force along the axis of the body. Similarly, the opposite in the direction of the side force at points i and ii in Fig. 5Ab is echoed in the reverse asymmetry in the pressure distributions shown in Figs. 13a and 13b. In Fig. 13c, the pressure distribution corresponding to the roll angle ($\phi = 43.2$ deg) at which the side force reaches a local minimum is presented. Here, the asymmetry in pressure

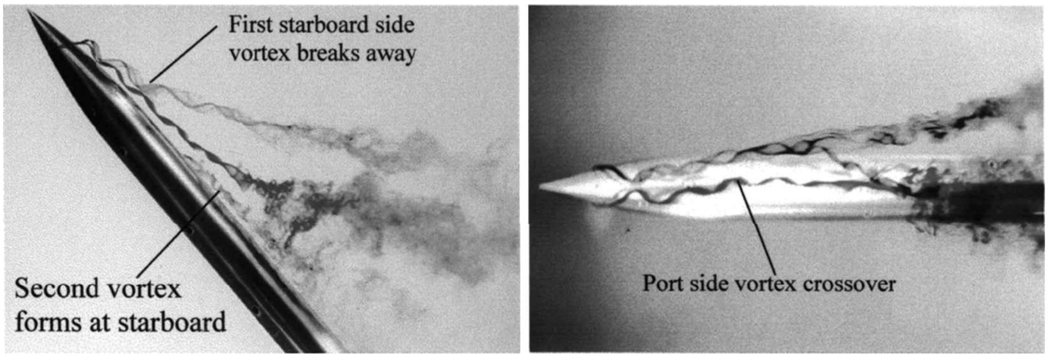

Fig. 15 Asymmetric vortex flow of tangent ogive cylinder at ϕ = 225 deg and α = 50 deg.

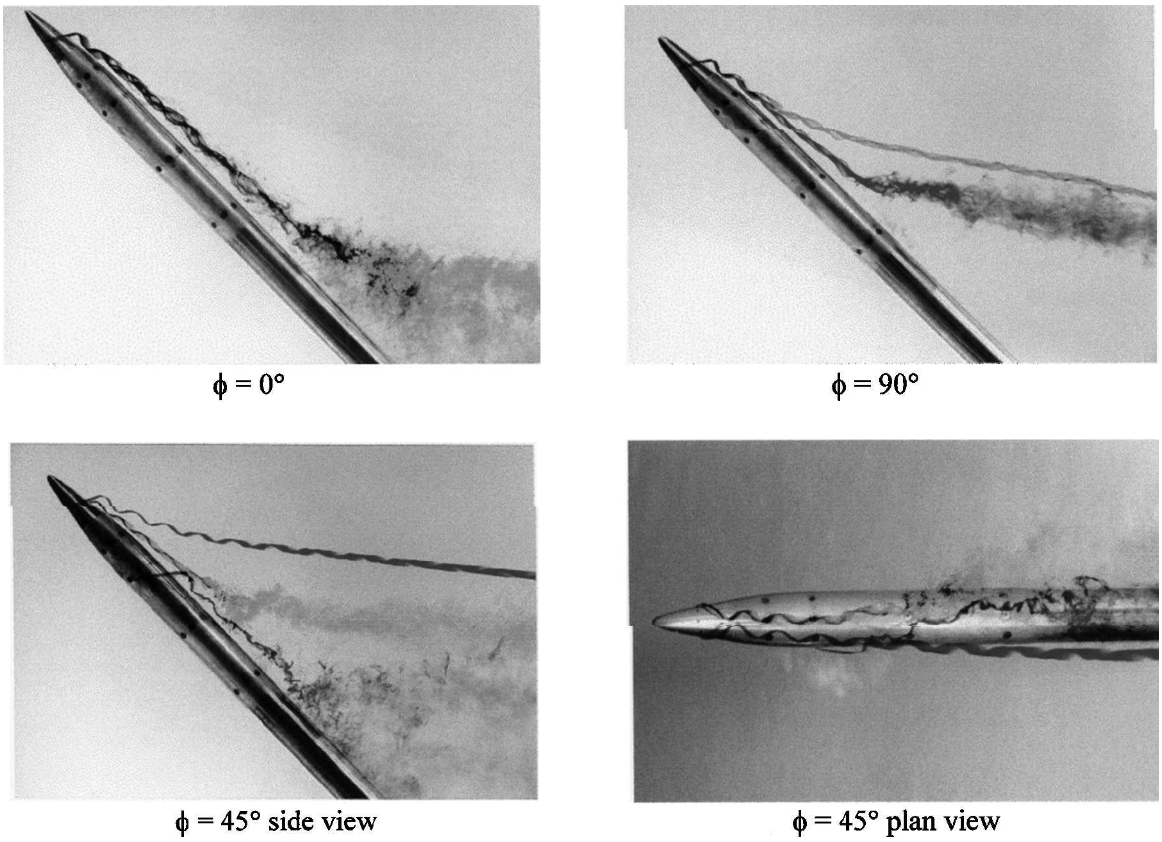
$\phi = 0°$

$\phi = 90°$

$\phi = 45°$ side view

$\phi = 45°$ plan view

Fig. 16 Flow past elliptical-tip cylinder at α = 45 deg.

distribution can be observed only in the first three stations, and there is no apparent variation in the side-force direction along the axis of the cylinder. At $\alpha = 80$ deg, the side force is back to nearly zero except at locations near $\phi = 0$ and 180 deg, where the side force still exhibits a step-like change in value (Fig. 5Bi). This behavior is not unlike the case of $\alpha = 70$ deg, although a slight change in magnitude is observed here. The pressure distribution corresponding to the small side force at $\phi = 43.2$ deg in Fig. 5Bi is shown in Fig. 14. The asymmetry in the pressure distribution appears to occur only in the first two stations, and the extent of the asymmetry is less than the asymmetries at lower angles of attack. Beyond the second station, the pressure distributions appear to be symmetrical and resemble those of a circular cylinder in a normal crossflow.

By comparing the side force acting on the ogive tip with that on elliptic tips, the following observations can be made. It is found that the nonzero side force occurs at a lower angle of attack for the elliptic tip than for the ogive tip. At the angles of attack of 20–30 deg, although the side force varies with the roll angle in a continuous manner for both tip shapes, the magnitude for the elliptic tip is found to be larger. However, once the side-force distribution with the roll angle exhibits a square-wave-like form at $\alpha \approx 40$–60 deg, the maximum side-force magnitude and the corresponding asymmetry in pressure distribution appear to be independent of the tip shape. Similar observation had been reported previously by Hunt and Dexter,[16] Dexter and Hunt,[17] and Zilliac et al.[27] In this range of α, the switching of the side force was found to be more predictable for the elliptic tip than the ogive tip. At large angle of attack of $\alpha \geq 70$ deg, the side force associated with the ogive tip is again negligible, whereas some step change in the side force can still be seen near $\phi = 0$ and 180 deg for the elliptic tip. This step change in side force is obviously undesirable.

Further tests were carried out to determine the effects of hysteresis and Reynolds number. For the hysteresis test, the model was rolled in both directions, and there is no evidence of hysteresis occuring in the present experiment. As for Reynolds number effects, unfortunately, only a limited range of Reynolds numbers can be studied because of the limited speed range in the tunnel.

Nevertheless, data collected at the Reynolds number that is two-thirds of the initial value show that the effect of the Reynolds number, if any, is negligible. However, this part of the test is not conclusive enough to suggest that the Reynolds number dependence is not presence.

C. Flow Visualization Results

In the present investigation, a fairly extensive flow visualization investigation was carried out to obtain further clues about the general flowfield around the models. Unfortunately, because of space constraints, a comprehensive discussion of the results is not possible; only the salient features of the structures are discussed. On the basis of the flow visualization results, it is reasonable to suggest that the presence of the side force is related to the asymmetric growth and the subsequent liftoff of the vortices from the two sides of the body. Further, as the angle of attack increases, the locations of vortex asymmetry, vortex breakaway, and vortex breakdown are found to propagate upstream toward the tip. An important point is that, when the body is at a moderate angle of attack ($\alpha = 40$ and 45 deg) and as it is rotated about its axis of symmetry, the flow pattern can change from an asymmetric configuration to a symmetric configuration and then to the opposite asymmetric orientation. Interestingly, at a larger angle of attack ($\alpha = 60$ deg), the symmetric configuration that exists between two asymmetric configurations detected at low α is absent. The flow pattern is at either one asymmetric configuration or the opposite asymmetric configuration. This observation seems to support the bistable behavior of the side-force distribution. A typical asymmetric state at $\alpha = 50$ deg is shown in Fig. 15. Here, it can be seen that the starboard-side vortex has lifted off earlier than the port-side vortex, and at the same time a second vortex is formed at the starboard side. From the plan view, it is found that, when the starboard vortex is lifted off from the body, there is a tendency for the port vortex to be induced by the velocity/pressure field of the lifted vortex, causing the latter to cross over the center plane of the cylinder. In this case, the local side force is expected to be negative (i.e., pointing toward the port side) near the nose tip, reaches a maximum at an axial location when the starboard vortex breaks away and changes its sign (i.e., points in the starboard side-force direction) when the port-side vortex crosses over and a new starboard vortex is formed. The overall side force is pointing in the port direction.

Figure 16 shows the flow pattern of the elliptical-tip model when $\alpha = 45$ deg, where the flow asymmetry and the crossover of vortices at different roll angles are depicted clearly. Note that, when $\phi = 0$ deg (major axis of ellipse transverse to freestream), the flowfield appears to be more symmetrical than that at $\phi = 90$ deg (minor axis transverse to freestream), which shows a rather large flow asymmetry. This behavior could be due to a larger separation (distance) between the two shear layers at $\phi = 0$ deg than that when $\phi = 90$ deg. The flow asymmetry becomes more pronounced when $\phi = 45$ deg. In this configuration, it can be seen that, when the port vortex breaks away, the starboard vortex is induced toward the cylinder centerline. The new port vortex that has formed is very distinct and extends to a large axial distance downstream.

IV. Conclusions

The main findings of the present investigation can be summarized as follows:

1) When the angle of attack is small ($\alpha \leq 10$ deg approximately), it is found that the side force generated on either an ogive-tip or an elliptic-tip cylinder is small, and the surface pressure distribution is symmetrical. When α is between 20 and 30 deg, the side force exhibits a sinusoidal distribution with the roll angle, with the elliptic tip cylinder being subjected to a side force with a larger magnitude. When α is increased further to about 40–60 deg, the side-force distribution becomes square wave like. Here, the force direction can change abruptly from one sign to the opposite sign. Note that, although the two different nose geometries have been used, their total side forces are almost the same. Beyond $\alpha = 70$ deg, the results show that the side forces have diminished.

2) For the elliptic tip, the sinusoidal and square-wave-like distributions of the side force appear to start at a slightly lower angle of attack than those for the ogive tip. Also, the distributions are found to be more predictable than that for the ogive tip, which is consistent with the earlier results of Moskovitz et al. and Bridges and Hornung. Here, the switchover of the side-force direction occurs at every $\phi = 0$, 90, 180 deg, etc. Moreover, when $\alpha > 70$ deg, there appears to be a slight discontinuity in the side-force distribution at $\phi \approx 0$ and 180 deg. This feature is not found on the ogive-tip nose.

3) Although only a limited number of pressure measurements have been taken, the results show that only when the body is at certain angle of attack and roll angle is there an axial variation of the local side force along the axis of the cylinder. Also, it appears that changes in the direction of the side force are related to the changes in the asymmetry of the pressure distribution along the body.

4) Over the limited range of Reynolds numbers ($Re_D = 2.3333 \times 10^4$–$3.5 \times 10^4$) investigated in wind tunnel, it appears that the aerodynamics of the ogive-tip cylinder are independent of the Reynolds number.

5) Flow visualization studies show that, when the angle of attack increases, the locations of vortex asymmetry, vortex breakaway, and vortex breakdown propagate upstream toward the tip. In addition, it is found that, at $\alpha = 45$ and 50 deg, the changes in the vortex structure with the roll angle occur in a more gradual manner; i.e., one can see a nearly symmetric flow pattern occurring between the two opposite asymmetric flow patterns. On the other hand, at $\alpha = 60$ deg, changes in the flow pattern with the roll angle are more abrupt, leading to the formation of a bistable state. Here, there is no evidence of the symmetrical flow pattern.

6) The elliptical tip with the major axis transverse to the freestream is found to be more effective in delaying the onset of the flow asymmetry to a higher angle of attack than when the minor axis is transverse to the freestream.

References

[1] Keener, E. R., and Chapman, G. T., "Onset of Aerodynamic Side Force at Zero Sideslip on Symmetric Forebodies at High Angles of Attack," AIAA Paper 74-770, Aug. 1974.

[2] Keener, E. R., Chapman, G. T., and Kruse, R. L., "Effects of Mach Number and Afterbody Length on Onset of Asymmetric Forces on Bodies at Zero Sideslip and High Angle of Attack," AIAA Paper 76-66, Jan. 1976.

[3] Coe, P. L., Chambers, J. R., and Letko, W., "Asymmetric Lateral-Directional Characteristics of Pointed Bodies of Revolution at High Angles of Attack," NASA TN-D-7095, Nov. 1972.

[4] Malcolm, G. N., and Ng, T. T., "Forebody Vortex Control as a Complement to Thrust Vectoring," Society of Automotive Engineers, TP Series 901851, 1990.

[5] Malcolm, G. N., "Forebody Vortex Control," AGARD R-776, 1991.

[6] Peake, D. J., and Owen, F. K., "Control of Forebody Three Dimensional Flow Separation," CP 262-15, AGARD, 1979.

[7] Rao, D. M., "Side-Force Alleviation on Slender, Pointed Forebodies at High Angles of Attack," *Journal of Aircraft*, Vol. 16, No. 11, 1979, pp. 763–768.

[8] Keener, E. R., Chapman, G. T., and Cohen, L., "Side Forces on a Tangent Ogive Forebody with a Fineness Ratio of 3.5 at High Angles of Attack and Mach Numbers from 0.1 to 0.7," NASA TM-X-3437, Feb. 1976.

[9] Keener, E. R., Chapman, G. T., Cohen, L., and Taleghani, J., "Side Forces on Forebody at High Angles of Attack and Mach Numbers from 0.1 to 0.7: Two Tangent Ogives, Paraboloid and Cone," NASA TM-X-3438, Feb. 1976.

[10] Stahl, W., "Suppression of Vortex Asymmetry Behind Circular Cones," *AIAA Journal*, Vol. 28, No. 6, 1990, pp. 1138–1140.

[11] Asghar, A., Stahl, W. H., and Mahmood, M., "Suppression of Vortex Symmetry and Side Force on a Circular Cone," *AIAA Journal*, Vol. 32, No. 10, 1994, pp. 2117–2120.

[12] Ng, T. T., "Effect of a Single Strake on the Forebody Vortex Asymmetry," *Journal of Aircraft*, Vol. 27, No. 9, 1990, pp. 844–846.

[13] Keener, E. R., and Chapman, G. T., "Similarity in Vortex Asymmetries over Slender Bodies and Wings," *AIAA Journal*, Vol. 15, No. 9, 1977, pp. 1370–1372.

[14] Rao, D. M., Moskovitz, C., and Murri, D. G., "Forebody Vortex Management for Yaw Control at High Angles of Attack," *Journal of Aircraft*, Vol. 24, No. 4, 1987, pp. 248–254.

[15] Ng, T. T., and Malcolm, G. N., "Forebody Vortex Control Using Small, Rotatable Strakes," *Journal of Aircraft*, Vol. 29, No. 4, 1992, pp. 671–678.

[16] Hunt, B. L., and Dexter, P. C., "Pressure on a Slender Body at High Angle of Attack in a Very Low Turbulence Level Air Stream," CP-247, AGARD, 1978 (Paper 17).

[17] Dexter, B. C., and Hunt, B. C., "The Effects of Roll Angle on the Flow over a Slender Body of Revolution at High Angles of Attack," AIAA Paper 81-0358, Jan. 1981.

[18] Champigny, P., "Side Forces at High Angles of Attack: Why, When, How?," *Recherche Aerospatiale (Aerospace Research)*, No. 4, 1994, pp. 269–282.

[19] Hunt, B. L., "Asymmetric Vortex Forces and Wakes on Slender Bodies," AIAA Paper 82-1336, Aug. 1982.

[20] Edwards, O. R., "Northrop F-5F Shark Nose Development," NASA CR-158936, 1978.

[21] Moskovitz, C. A., Hall, R. M., and DeJarnette, F. R., "New Device for Controlling Asymmetric Flowfields on Forebodies at Large Alpha," *Journal of Aircraft*, Vol. 28, No. 7, 1991, pp. 456–462.

[22] Moskovitz, C. A., Hall, R., and DeJarnette, F., "Experimental Investigation of a New Device to Control the Asymmetric Flowfield on Forebodies at Large Angles of Attack," AIAA Paper 90-0069, Jan. 1990.

[23] Bridges, D. H., and Hornung, H. G., "Elliptic Tip Effects on the Vortex Wake of and Axismmetric Body at Incidence," *AIAA Journal*, Vol. 32, No. 7, 1994, pp. 1437–1445.

[24] Lamont, P. J., "Pressure Around an Inclined Ogive Cylinder with Laminar, Transitional, or Turbulent Separation," *AIAA Journal*, Vol. 20, No. 11, 1982, pp. 1492–1499.

[25] Lamont, P. J., and Hunt, B. L., "Pressure and Force Distributions on a Sharp-Nosed Circular Cylinder at Large Angles of Inclination to a Uniform Subsonic Stream," *Journal of Fluid Mechanics*, Vol. 76, No. 3, 1976, pp. 519–559.

[26] Tajfar, A. H., and Lamont, P. J., "Sideslip Behavior of Elliptic Cross-Sectional Forebodies at High Angle of Attack," *Journal of Aircraft*, Vol. 34, No. 4, 1997, pp. 472–478.

[27] Zilliac, G. G., Degani, D., and Tobak, M., "Asymmetric Vortices on a Slender Body of Revolution," *AIAA Journal*, Vol. 29, No. 5, 1991, pp. 667–675.

A. Plotkin
Associate Editor